Journal Pre-proof

Validation of CFD-DEM simulation of a liquid–solid fluidized bed by dynamic analysis of time series

Julia Picabea, Mauricio Maestri, Miryan Cassanello, Gabriel Salierno, Cataldo De Blasio, María Angélica Cardona, Daniel Hojman, Héctor Somacal

PII: S1674-2001(21)00221-2

DOI: https://doi.org/10.1016/j.partic.2021.11.003

Reference: PARTIC 1557

To appear in: *Particuology*

Received Date: 10 June 2021

Revised Date: 27 October 2021

Accepted Date: 12 November 2021

Please cite this article as: { doi: https://doi.org/

Validation of CFD-DEM simulation of a liquid–solid fluidized bed by dynamic analysis of time series

Julia Picabea [1,2], Mauricio Maestri [1,2], Miryan Cassanello [1,2], Gabriel Salierno [1,3,5,*], Cataldo De Blasio [3], María Angélica Cardona [4,5,6], Daniel Hojman [4,5], Héctor Somacal [4,6]

[1] Departamento de Industrias, Facultad de Ciencias Exactas y Naturales, Universidad de Buenos Aires; Intendente Güiraldes 2160 - Ciudad Universitaria - C1428EGA - Buenos Aires, Argentina

[2] CONICET-Universidad de Buenos Aires, Instituto de Tecnología de Alimentos y Procesos Químicos – ITAPROQ; Intendente Güiraldes 2160 - Ciudad Universitaria - C1428EGA - Buenos Aires, Argentina

[3] Faculty of Science and Engineering, Åbo Akademi University, Rantakatu 2 - 65100 - Vaasa, Finland

[4] Laboratorio de Diagnósticos por Radiaciones, Dep. Física Experimental, Comisión Nacional de Energía Atómica, BKNA1650 San Martín, Buenos Aires, Argentina

[5] CONICET, C1033AAJ Buenos Aires, Argentina

[6] Escuela de Ciencia y Tecnología, Universidad de San Martín, BKNA1650 San Martín, Buenos Aires, Argentina

* Corresponding author. E-mail address: gabriel.salierno@gmail.com (G. Salierno)

Graphical abstract

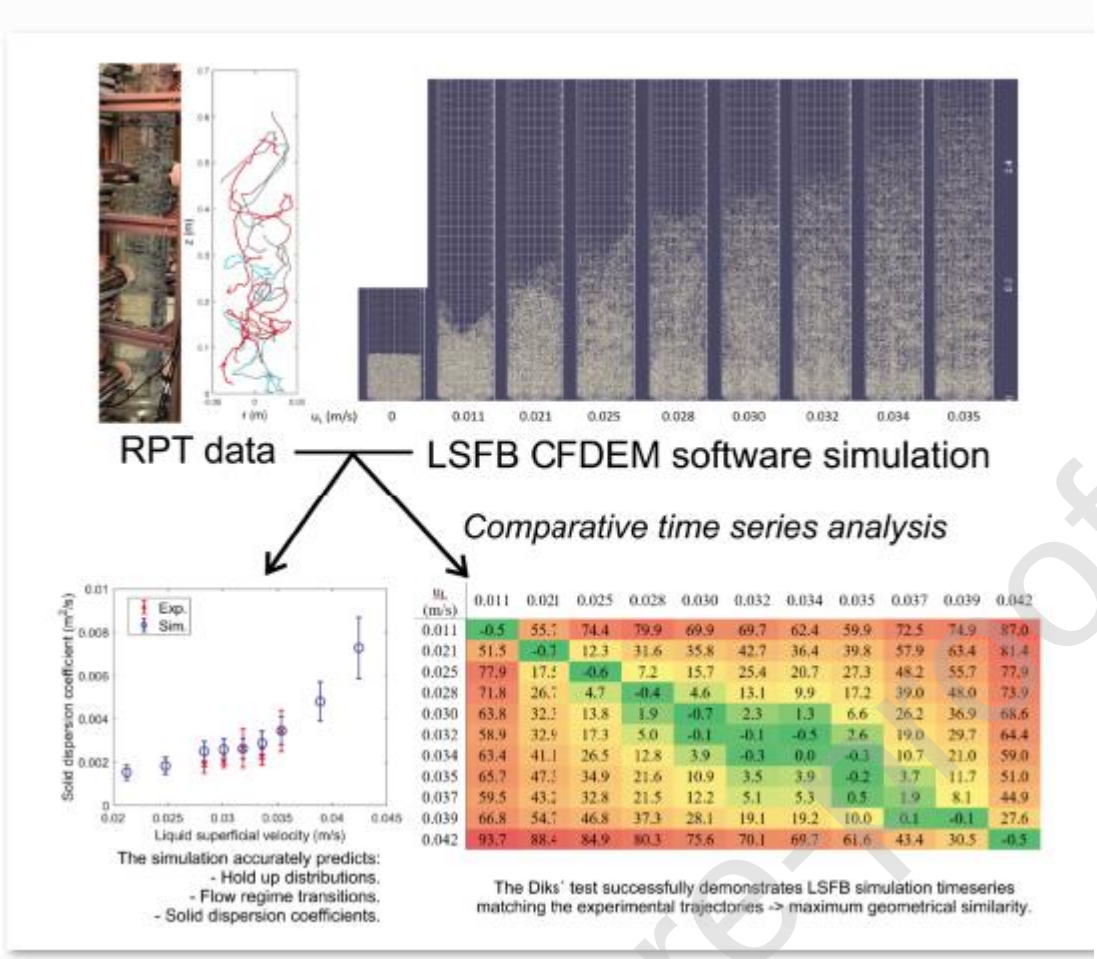

Highlights

- Diks' test indicates dynamic similitude of experimental and CFD-DEM simulated data.
- Observed flow regime transition is also identified solely from the simulations.
- Simulation predicts solid dispersion coefficients accurately.
- Solid mixing times, obtained from information entropy, differ less than 25%.

Abstract

Liquid–solid fluidized beds (LSFB) modeling validation is crucial for establishing design rules and monitoring tools. However, it generally relies on comparing global variables, which overlook dynamic features that influence reaction outputs. This work aims to implement time series analysis tools to compare

Radioactive Particle Tracking data with a simulation consisting of Computational Fluid Dynamics coupled with Discrete-Element Method. Experiments have been performed in a pilot-scale LSFB of calcium alginate spheres fluidized with a calcium chloride solution. The Diks' test indicates that the simulation can capture the LSFB behavior. It also allows diagnosing flow regime transitions from the simulation. Trends of solid dispersion coefficients and mixing times predicted by the simulation are in good agreement with the experiments.

Keywords: Liquid–solid fluidization, CFD-DEM, Dynamic comparison, Radioactive Particle Tracking

Nomenclature

Latin symbols

C_d Drag coefficient (-)
d Diameter (m)
d Time-series bandwidth (-)
D Dispersion coefficient (m^2/s)
E_{peak} Radiotracer peak emission energy (keV)
f Force (N)
g Acceleration of gravity (m/s^2)
L Number of segments from a time series (-)
m Particle mass (Kg)
m Embedding dimension (-)
n Number of particles within a voxel (-)
N Number of bins of a probability simplex (-)
p Probability (-)
p Pressure (Pa)
r Radial coordinate (m)
$\boldsymbol{R}$ Internal coordinate of an attractor
Re Reynolds number
S Diks' S-statistic (-)
Q Distance estimator between attractors (m)
t Time (s)
$t_{1/2}$ Radiotracer half-life (days)
u Local liquid velocity (m/s)
u_L Superficial liquid velocity (m/s)
v Particle velocity (m/s)
V Particle volume (m^3)
V_c Conditional variance (m^2)
x x-coordinate (m)
$\bar{x}$ Position vector (m)
X Delay-vector
y y-coordinate (m)
z Height (m)
Z Column height (m)

Greek symbols

α Hold-up (-)
χ Di Felice drag model parameter (-)
ε Local volume fraction (-)
Φ Attractor
μ Viscosity (Pa·s)
ρ Density (kg/m^3)
π Pi number (-)
τ Shear stress tensor (m^2/s^2)
τ Manifold period (s)
ξ Mean displacement (m)
Ω Normalized Shannon entropy (-)

Operators

δ Finite derivative
∑ Finite summation

∇ Gradient
$\nabla \cdot$ Divergence
$|\cdot|$ Norm of a vector

Subscripts
c Plastic collision
d Drag
e Elastic collision
i i-th particle
j j-th particle
k k-th component of a delay vector
κ κ-th bin of a probability simplex
L Liquid phase
o Initial
p Particule
pL Particle–liquid interaction
s Solid phase
$\nabla \mathbf{p}$ Pressure gradient
$\nabla \cdot \boldsymbol{\tau}$ Shear

1 Introduction

Liquid–solid fluidized beds are utilized in many industrial processes and operations (Di Felice, 1995; Kramer et al., 2019). This equipment is easy to mount and presents outstanding heat and mass transfer characteristics (Khan et al., 2020). However, unit design and operation are complex due to the entangled hydrodynamics (Wang et al., 2012). Understanding and describing the underlying dynamics is crucial for establishing robust design rules and monitoring tools with suitable predictive capacity (Al-Juwaya et al., 2019; Duduković and Mills, 2015).

Methods for studying fluidization dynamics should not alter the flow of the phases when making the measurement; that is, they must be "non-invasive" (Ali et al., 2015; Duduković and Mills, 2015). One of the most significant challenges in analyzing the movement of the phases is finding appropriate tracers to represent them along with analytical techniques that allow measurement "in situ" without extracting a sample to avoid altering the movement. In the last few decades, experimental methods have been developed to determine trajectories of freely moving particles within multiphase equipment (Wang, 2015). Among them, the Radioactive Particle Tracking (RPT) technique provides comprehensive information on the movement of solids at a pilot-scale (Al-Juwaya et al., 2019; Roy et al., 2005; Salierno et al., 2013). This specific application can extract macroscopic information of industrial interest in generally opaque conditions and present complex rheology.

In addition to the insights gained from the experimental studies of fluidized systems, the simulation of the motion in each phase allows interpreting the results and predicting diverse flow patterns. Computational Fluid Dynamics coupled with Discrete Element Method (CFD-DEM) models are proven to be entirely appropriate in representing the solid and liquid motion in fluidized beds (Hager et al., 2018; Hua et al., 2020). Validation by comparison with experimental results has generally used global or time-

averaged variables (Hager et al., 2014). However, several dynamic behaviors can lead to similar mean profiles, while in many cases, reaction outputs rely on time dependence, especially for relatively fast processes (Zou et al., 2019). Moreover, fluidized beds are considered chaotic (Kalo et al., 2019) since their dynamic can be explained by applying Newtonian laws of motion with immeasurable degrees of freedom. Therefore, linear statistics are unable to capture detailed dynamical features of the highly variable particle trajectories. For that, simulations frequently suffer from appropriate validation due to the difficulty in determining the motion of the intervening phases (Duduković and Mills, 2015; Goniva et al., 2012; Kalo et al., 2019; Roy, 2017). Nonlinear time series analysis based on chaos theory is more suitable to characterize the time evolution of a complex system (Zou et al., 2019), such as bubble columns (Ebrahimi-Mamaghani et al., 2019) or fluidized beds (Lichtenegger, 2018; Zhang et al., 2021), among other multiphase systems in a turbulent flow. A proper characterization of complex systems provides the discrimination of distinctive features and the prediction of regime shifts (Zou et al., 2019). Additionally, non-linear time-series analysis is a powerful tool for verifying and validating models dedicated to the detailed simulation of fluidized beds.

This work aims to compare results obtained by CFD-DEM simulation with those arising from RPT using time series analysis tools. The experiments have been performed in the Radiation Diagnosis Laboratory belonging to the Argentine Atomic Energy National Commission (CNEA), in a pilot-scale liquid–solid fluidized bed sweeping a range of liquid velocities between the minimum fluidization and the transition to circulation. The motion of calcium alginate spheres induced by the upward flow of a diluted calcium chloride solution was inspected and simulated. Calcium alginate-water systems can be found in processes involving immobilized enzymes or microorganisms (Ercole et al., 2021; Liu et al., 2021). Liquid–solid fluidized beds with gel particles are also employed to purify proteins, adsorb waterborne contaminants, and as catalyst support (Bennacef et al., 2021; Platero et al., 2017; Sutirman et al., 2021; Wang et al., 2018).

The influence of operating conditions and simulation parameters was assessed to validate the model. Trends of statistics quantifying the chaotic features of the motion were determined both from the experiments and the simulation. In chaotic systems in a pseudo-steady-state, the trajectory in a multidimensional phase space tends to a set of zero volume in phase space: an attractor. The Diks' test (Diks et al., 1996) ability to quantitatively compare subtle differences between attractors describing the underlying dynamics was applied to study the liquid velocity influence. The simulated data were also analyzed with the same tools within an extended range, and the results were compared. Lastly, solid dispersion coefficients and mixing times predicted by the CFD-DEM model are successfully verified by comparison with RPT data.

2. Experimental section

Experiments were carried out in an acrylic column (1.2 m height and 0.1 m inner diameter), provided with a multi-hole liquid distributor of 0.022 open area ratio. The liquid phase is an aqueous solution of $CaCl_2$ (0.05 M), flowing in a closed-loop impelled by a centrifugal pump moderated by a diaphragm valve. The liquid superficial velocity (u_L) is set and controlled at different constant values between 800 and 1000 L/h (0.028 to 0.036 m/s of superficial liquid velocity), 25% above the minimum fluidization velocity and 25% below the circulation velocity. Liquid velocities are chosen within the stable fluidization range: above the minimum fluidization velocity and below the minimum circulation velocities. For safety reasons regarding the radiotracer handling, no experiments were performed above circulation velocities. Below the minimum fluidization velocity, the system behaves as a fixed bed, and the RPT data would have no informative value.

Calcium alginate beads of 4 mm mean diameter were the fluidized solids. They were generated by dropping aqueous calcium alginate 1.5% into 0.5 M aqueous calcium chloride under gentle agitation. The bed height at rest represented 8% of the total column height, and the solid to liquid density ratio was 1.02. Characteristics of the liquid and solid phases and the tracer are detailed in Table 1.

Table 1

A schematic of the facility is shown in Fig. 1. The radioactive tracer used to follow the solid motion was prepared to match the suspended gel particle size, density, texture, and wettability. It was made by embedding a 7µg piece of gold, previously sealed into a 1mm polypropylene sphere and activated by neutron bombardment to ^{198}Au ($t_{1/2}$=2.7d, E_{peak}=412 keV) in the RA1 reactor of the CNEA. After activation, it was covered with calcium alginate in a mold (Salierno et al., 2018). To perform the RPT measurements, we devise an array of conveniently distributed 16 (2" × 2") NaI (Tl) scintillation detectors surrounding the column (Fig. 1) and the required electronics. To achieve the reconstruction of the tracer trajectory, it is necessary to estimate what would be the set of signals registered by the detectors when the tracer is in different positions of the equipment. The reconstruction of the tracer trajectory is carried out from the knowledge of the expected count in each detector when the radioactive source is located in different positions of the reactor. That is, we must have a “dictionary” that associates each position of the tracer with a set of counts in the detectors. The dictionary is constructed knowing the geometry of the reactor-detection system, the activity of the radioactive source, the attenuation coefficient of the medium, and the absolute efficiency of each detector for each position of the tracer. The tracer is tracked for several hours at a sampling period of 30 ms.

Fig. 1

For the tracer trajectory reconstruction, a calibration stage was conducted preceding the experiment by determining the counts recorded by each detector when the tracer is positioned at known coordinates within the system. A detector response function was modeled by the Monte Carlo method that considers

the signal distribution (in the form of a detected number of gamma photon counts), the tracer radioactivity, the media attenuation coefficient, and the dead time of each detector. By comparing the combined detector response for a several locations in the column with the actual values measured when the tracer is moving, the tracer position while freely moving in the column is calculated. Further details of the reconstruction procedure can be found in Chaouki, Larachi, and Dudukovic (1997).

3. Liquid–solid fluidized bed CFD-DEM model implementation

The open-source CFDEM® software (Hager et al., 2018) on the Linux platform was used for the CFD-DEM simulations. The Navier-Stokes equations were solved numerically by OpenFOAM with the Solver Pressure-Implicit with Splitting of Operators (PISO) to describe the liquid motion. LIGGHTS was used for simulating the motion of 13500 solid particles. The optimum mesh was on the order of 3 times the particle diameter (Maestri et al., 2019). Results were visualized using ParaView. For the solid phase, the forces acting on the particles (gravity, buoyancy, drag, solid–solid, and liquid–solid interactions) were calculated, according to the proposal of (Wang et al., 2012). The proposed strategy calculates momentum exchange between the liquid (Eq. (1)) and the solid particles (Table 2).

$$\delta(\rho_L \varepsilon_L \mathbf{u})/\delta t + \nabla \cdot (\rho_L \varepsilon_L \mathbf{u}\mathbf{u}) = -\boldsymbol{\nabla}\mathbf{p} - [n\mathbf{f}_\mathbf{i}'/\varepsilon_L - \rho_L \varepsilon_s \mathbf{g}] + \boldsymbol{\nabla}\cdot\boldsymbol{\tau} + \rho_L \varepsilon_L \mathbf{g} \quad (1)$$

ρ_L, ρ_s, ε_L and ε_s are density and volumetric fractions of liquid and solid respectively, **u** is the local average velocity of the liquid, $\mathbf{v_i}$ the local velocity of individual particles, p is the local pressure field, $\boldsymbol{\tau}$ is the local stress tensor, n is the local number of particles per unit volume, $\mathbf{f'_i}$ is the local average force on the particles, m_i is the mass of the i-th particle, $V_{p,i}$ is the particle volume, $d_{p,i}$ is the particle diameter, μ_L is the liquid dynamic viscosity, and **g** is the acceleration of gravity.

Table 2, 3

Table 3 summarizes the simulation parameters. An unresolved CFD-DEM scheme is implemented with a Cartesian structured mesh of 0.9 cm^3 size. Numerical CFD stability was validated a priori procuring a Courant-Friedrichs-Levy (CFL) number several orders of magnitude lower than 1 for the superficial liquid velocity and maximum liquid interstitial velocity in every operating condition. Lubrication forces are omitted after evaluating a very low impact on the results while significantly increasing the computational time. Turbulent structures were taken into account using a k-epsilon model (Maestri et al., 2019).

4 Results and discussion

Solid hold-up distribution and velocity fields calculated from the simulation are compared with experimental results obtained with RPT. Furthermore, parameters used to characterize time series are

calculated to assess the time-dependent behavior of the trajectory and contrast experimental results with simulations. The underlying attractors describing the dynamics of each condition are obtained from the experiments and characterized by computing the correlation dimension and the Kolmogorov entropy (van Ommen et al., 2011). The Diks' test is used to determine, from the tracer coordinate time series, if there is a flow regime transition within the explored velocity range, as proposed by Fraguío et al. (2007). It is applied to both experimental and simulated data. The dispersion coefficients are determined by considering the Einstein relation to a manifold of trajectories starting from given locations, both using the experimental and simulated data, to analyze the prediction capacity of the simulation. Solid mixing times are assessed using information theory and compare results arising from experimental and simulated data.

4.1 Probabilities and phase distribution

Considering that the tracer freely moves within the fluidized bed, and assuming the condition of ergodicity, the distribution of solids in the column can be estimated from the probability distribution of its presence at different locations. The probability distribution is obtained from the path determined by RPT, and it is related to the solid holdup for different locations, $\alpha_s(\overline{x_i})$, as expressed in Eq. (2) where $\alpha_{s,o}$ is the mean solid holdup for each experimental condition.

$$\alpha_s(\overline{x_i}) = \alpha_{s,o} \cdot p(\overline{x_1}) \qquad (2)$$

Where $p(\overline{x_1})$, in the case of the RPT data, is the normalized frequency of the events where the tracer is in the voxel centered at the position $\overline{x_i}$. In the case of the CFD-DEM simulations, $p(\overline{x_1})$ is the time-averaged probability of finding particles within the voxel $\overline{x_1}$. The solid holdup axial profiles are calculated from the experimental trajectories and compared with those obtained from the simulations. Fig. 2 shows a solid hold up profile comparison for three representative conditions. The simulations provide higher values of the axial profile (Fig. 2(a)) in the column base. The axially averaged radial profile (Fig. 2(b)) present good agreement between the experiment and that predicted by simulation. Dissimilarities observed in the lower zone of the axial profile might be due to an artifact introduced by the inaccuracy in capturing the proper drag in the region close to the liquid distributor, which provokes an accumulation of restrained particles at the bottom zone of the column wall, as can be observed in Fig. 2(c). Also, the tracer might suffer a hindrance to reaching the top of the column. However, the mean trends are comparable.

Fig. 2

The solid holdup decreases along with the column height, being quite low close to the fluidized bed upper limit. In the lower part of the column, it decreases as the liquid velocity increases. Axially averaged radial profiles are not affected by liquid velocity. The experimental results might indicate particles of slightly different densities since there are two regions of hold-ups. This apparent divergence between the experimental and simulated solid hold-up axial profiles can be explained by the compromise that must be

reached when a single radioactive tracer trajectory obtained by RPT is compared with multiple simulated trajectories.

The profile shape is probably related to the overall size and density distributions of the alginate beads obtained by the preparation technique, which is generally around 20% (Lee et al., 2013). It is not considered in the simulation. The predicted solid hold-up at the top of the column is lower than the experimental results, thus slightly underestimating the bed expansion. On the contrary, the solid hold up close to the upper limit is higher than the experimental for the highest liquid velocity, thus slightly overestimating the bed expansion for this condition. The solid hold-up obtained by simulation is higher than the experimental one in the column base, although the liquid distribution geometry was considered.

4.2 Velocity Fields and solid motion features

Instantaneous velocities were calculated from the tracer trajectory obtained from RPT. The column is discretized in voxels, and the velocity of the tracer, whenever crossing each voxel, is computed and then time-averaged to get the 3D velocity field. From the simulations, 3D velocity fields can also be obtained considering the same column discretization and computing the particle velocity crossing the different voxels at different times. Fig. 3 presents the radial-axial projection of the solid velocities determined by azimuthally averaging the 3D velocity field obtained from the experiments and simulations.

Fig. 3

For high liquid velocities, the general pattern indicating a toroidal vortex structure, with faster upward motions close to the center of the column and downward motions shifted to the column wall, is apparent in both the experimental and simulated velocity fields. However, the experiments show less definite patterns, indicating that the fast-ascending paths might be located in a different region in the simulations. The simulation displays more definite circulation in the column base and could be due to the motion hindrance of the tracer at the entrance near the column wall. In the case of low liquid velocities, the particle velocities are significantly less intense, and the toroidal motion pattern is less evident.

4.3 Diks' test

The conventional statistical analysis fails to identify similarities or differences regarding the origin of two time series (Zou et al., 2019), the dynamics in the series that often get smoothed when global or time averages are studied. In these cases, comparing the reconstructed attractors of two systems can determine whether the same mechanisms generate them.

A delay-vector attractor (Eq. (3)) can be obtained from the time series of observables representing a characteristic variable of the series. For a series of length N_t values, a set of $(N_t - m + 1)$ delay-vectors X_k of dimension m can be extracted according to Eq. (3).

$$X_k = \left(x_k, x_{k+\tau}, x_{k+2\tau}, \ldots, x_{k+(m-1)\tau}\right), \quad k = \{1, \ldots, N-m+1\} \tag{3}$$

The attractor representing the underlying dynamics of the system can be reconstructed from the time evolution of these vectors. These delay-vectors can be seen as points in an m-dimensional space that form the reconstructed attractor $\Phi\,(X)$. Takens (1981) showed that the attractor keeps the original dynamical features of the system to be used as a footprint. The distance Q between attractors can be expressed as in Eq. (4).

$$Q = (2d\sqrt{\pi})^m \int (\Phi_x(\boldsymbol{R}) - \Phi_y(\boldsymbol{R}))^2 d\boldsymbol{R} \tag{4}$$

Diks et al. (1996) provide an estimator $\hat{Q}$ of Q and propose a statistic S for testing the null hypothesis that two sets of vectors are drawn from the same multidimensional probability distribution defined in Eq. (5):

$$S = \frac{\hat{Q}}{\sqrt{V_c\,(\hat{Q})}} \tag{5}$$

where V_c is the conditional variance of $\hat{Q}$. The test involves selecting four parameters: the length of the time series, the embedding dimension, m, the bandwidth, d, and the number of segments, L (Fraguío et al., 2007; van Ommen et al., 2011, 2000). A set of (N_t–m) delay vectors of dimension m can be extracted from the time series of a system characteristic variable of N_t values. Comparing the attractors reconstructed from two time series can determine whether the same mechanism has generated them. Hence, *S* quantifies the difference between attractors and provides a quantitative mean of comparing the dynamics of the systems.

Diks' test establishes that when the *S* statistic gives values below an arbitrary threshold, the null hypothesis is accepted; thus, the underlying dynamics are considered the same. As *S* is assumed to have zero mean and standard deviation equal to one, with a unimodal distribution, a cut-off value of $S = 3$ would imply a confidence level of 95%, based on the 3σ rule (Diks et al., 1996; van Ommen et al., 2011). As *S* increases, there is more certainty that the same mechanism did not generate the two time series.

In this case, the test is first applied to the tracer axial coordinate experimental time series to diagnose if a flow regime transition is apparent within the liquid velocity range examined, as proposed by Fraguío et al. (2007) for three-phase fluidized beds. The test parameters proposed as optimal by Fraguío et al. (2007), m=20, L=33, d=1, were used to calculate the S-statistic. Fig. 4 shows the comparison within experimental data, taking different experimental conditions as references.

Fig. 4

When the experimental series for different liquid velocities are compared, results suggest that a flow transition occurs around 0.030-0.032 m/s. This is apparent regardless of the experimental condition taken

as reference. For applying the test to the simulated data with the same frequency as the experimental data, a very long path is required, which would take an extremely long computation time. Hence, assuming the hypothesis of ergodicity, the trajectory of one particle is reconstructed from the trajectory of several particles. Specifically, to start the time series, one particle is chosen randomly and followed from a given time, taken as time zero, for half a minute with the same sampling period as the one used for the experiments. Then, the region where the particle trajectory ends is observed when taken as time zero to search for another particle in the neighborhood moving in the same direction and with a similar velocity. The second chosen particle trajectory is thus concatenated to the first one, and the procedure is repeated until a time series of around a million events is reconstructed. In this way, sufficiently long time series for the analysis are obtained from simulations, of typically three minutes. Fig. 5 presents the S-statistic obtained by comparing the experimental and the thus obtained simulated time series, taking the experimental ones as references. As observed, the results are remarkably similar to those obtained from comparing within RPT data, indicating that the simulations capture the underlying dynamics of the experiments.

Fig. 5

Since the simulations seem to properly capture the underlying dynamics of the experiments, a comparison within simulated data is performed to check if the flow transition arising from the experimental results can be identified directly from simulations without comparison with an experimental reference. To search for flow transitions, the simulation is carried out for an extended liquid velocity range. First, the liquid velocities are swept to determine, from simulations, the condition of incipient fluidization. It is found that the simulation predicts 25% expansion above the height at rest for liquid velocities around 0.01 m/s. After corroborating from visual observations that a similar expansion is apparent in the experimental facility at this velocity, simulations are performed within the liquid velocity range spanning from 0.011 to 0.042 m/s. For the conditions at the highest liquid velocities, many particles are already transported, i.e., elutriated from the bed.

From applying the S-statistic within simulated results, Fig. 6(a) presents comparable results to those observed in Fig. 4(a), pointing to a flow transition around a liquid velocity of 0.03–0.032 m/s. It is also observed that for liquid velocities larger than 0.037 m/s, $S >> 3$ rapidly. Hence, within the range of 0.03 to 0.037 m/s, the Diks' test applied on the simulated data indicates that the underlying dynamics are similar and correspond to the same flow regime. In this case, according to visual observation of the experiments and simulations videos, the flow regime would be smooth homogeneous fluidization, with low particle-particle interactions. Fig. 6(b) illustrates the S-statistics behavior when the reference time series considered is at very low or high liquid velocity with respect to the minima region, shown in Fig. 6(a). For these reference conditions, $S < 3$ only when the time series is compared to itself; each condition is statistically different from all the others. Observing the S-statistic trend when considering the particle axial coordinate time series at a low liquid velocity, two breaks are observed in the trend around 0.03–0.032 m/s and above

0.037 m/s (marked with a dashed line), in coincidence with the results shown in Fig. 6(a). Hence, the first break would correspond to the attainment of complete stable fluidization, and the other from 0.037 m/s, indicating the onset of solid entrainment.

Fig. 6

When the reference is in a high liquid velocity condition, it is also observed but less marked. Apparently, it is more convenient to use, as a reference, a time series in a region of stable fluidization instead of values close to the fluidization limits, i.e., for incipient entrainment or close to the minimum fluidization velocity. The appearance of this fluidization regime has been suggested by Sheikhi et al. (2013) from vibration and pressure fluctuation analysis in a liquid fluidized bed. These authors called it solid fluidization regime. The resulting S statistics obtained when comparing within simulated data are shown in Table 4, marked as green when the dynamic similarity hypothesis is accepted under the 3σ rule and orange/red when it is rejected.

Table 4

The lowest values were expected to be at the diagonal. However, within the range between 0.032 and 0.037 m/s, the coincidence region becomes broader and would provide another way of defining the stable homogeneous fluidization flow regime limits. Out of this region, the time series compares well only with itself. Fig. 7 illustrates snap-shots of the simulations for an instant after three minutes for a broad range of liquid velocities. The figure shows that the particles are well dispersed for liquid velocities larger than 0.03 m/s, except in the region very close to the entrance. Below this velocity, the simulation predicts regions of different densities and a less uniform upper limit.

Fig. 7

For comparison, Fig. 8 shows photographs of the fluidized bed corresponding to the lowest and highest liquid velocities examined with RPT. The bed is denser in the lower level of the column ($z/Z < 0.5$) for a liquid velocity of 0.028 m/s. On the contrary, particle distribution is uniform in the whole column for a liquid velocity in the range corresponding to the flow regime predicted by the simulations.

Fig. 8

4.4 Correlation dimension and Kolmogorov entropy

The correlation dimension and the Kolmogorov entropy characterizing the attractors obtained from delay vectors of the time series have been extensively used as a means to detect a flow regime transition. Either pressure fluctuations (van Ommen et al., 2011) or the coordinate of a moving particle tracer determined by RPT (Cassanello et al., 1995) have been used, among other characteristic variables.

Schouten, Takens, and van den Bleek (1994a; 1994b) have proposed robust methods for estimating the correlation dimension and the Kolmogorov entropy from noisy time series. These methods were applied to the experimental and the simulated data, and the results are shown in Fig. 9. Absolute values of the parameters obtained from experimental data differ from those calculated from the simulations. However, a break in the correlation dimension trend is apparent in both cases for a liquid velocity around 0.03–0.032 m/s (Fig. 9, left). The break is scarcely observed in the Kolmogorov entropy trend determined from the simulations and not distinguished in the experimental data. Recently, Lichtenegger (2018) implemented a recurrence analysis of local solid concentrations to distinguish between flow regimes in a laboratory-scale two-dimensional gas-solid fluidized beds monitored by optical methods and successfully verified a two-dimensional CFD-DEM model also implemented in OpenFoam®. The results arising from applying the Diks' test and the work of Lichtenegger (2018) are significantly more conclusive in terms of CFD-DEM model verification.

Fig. 9

4.5 Solid dispersion coefficient

The dispersion coefficient (*D*) of fluidized solid particles can be estimated from the Einstein relation (Eq. (6)) for the divergence of trajectories of molecules, considering their equivalence with a diffusion coefficient exceeding the correlation time of Lagrange.

$$D = \frac{1}{2\tau}\langle \xi^2 \rangle_{(\tau)} = \frac{1}{2\tau}\sum_i \left(\left| \bar{x}_{i(\tau)} - \overline{x_o} \right| \right)^2 \qquad (6)$$

Where $\langle \xi^2 \rangle_{(\tau)}$ is the mean squared displacement with center at the initial point x_o after a period $\tau = t - t_o$ where t_o is the initial time of each trajectory. The mean squared displacement is estimated from the variance of many trajectories starting from x_o at $\tau = 0$, as suggested by Monin, Jaglom, and Lumley (1981).

We first construct a manifold of trajectories to calculate the solid dispersion coefficient from the tracer trajectory obtained by RPT. Again, it implies the discretization of the space in parcels or voxels and the use of the ergodicity hypothesis to get trajectories of different particles from extracts of the trajectory of a single particle at different times. We interpret these manifolds as injections of particles at a given region of the space (Salierno et al., 2018). The manifold of simulated trajectories is directly built by taking the path of different particles starting from the same voxel. From the manifold of trajectories obtained for each relevant voxel, every Euclidean distance to the starting point is determined. Fig. 10 represents the variance time evolution for a manifold, highlighting the linear zone after the correlation time of Lagrange. The slope of the highlighted points is considered as the solid dispersion coefficient multiplied by two.

Fig. 10

Subsequently, the mean squared displacement tends to be relatively constant since the particles move within a limited space. The solid axial dispersion coefficient is then determined from the maximum slope like the one illustrated in Fig. 10. It represents the linear relationship between the particles mean squared displacements from the injection point and τ. It must be verified that the number of trajectories considered is significant to guarantee confidence in determining the variances at each time. Fig. 11 shows an excellent agreement between the dispersion coefficients determined from the experimental tracer displacements with those predicted using the CFD-DEM simulation results.

Fig. 11

Up to 0.032 m/s, the influence of the liquid superficial velocity on the solid dispersion coefficients estimated from the experiments is minor. A slightly positive influence is observed above this limit. The simulations also point to a minor influence of the liquid velocity, which becomes significant when the particles start to be entrained (for u_L > 0.037 m/s).

4.6 Shannon entropy and mixing behavior

Information entropy can be utilized as an estimator for measuring the degree of randomness of solid particles in suspension from RPT data (Salierno et al., 2018). In this work, we use a normalized form of Shannon entropy as a statistic that estimates the homogeneity of a probability simplex applied to the chance of finding a particle representing suspended solids within fluids in motion, which can be used as a mixing index (Salierno et al., 2013; Van den Broeck and Esposito, 2015). The normalized Shannon entropy is a property of any discrete probability distribution, or simplex, $\{p_\kappa\}$ / $\kappa \in (1; \ldots; N)$, where N is the number of bins into which the distribution is divided. In the context of RPT, the valid range of the probability distribution will be the space that the tracer trajectory covers, and the bins will result from the granularity with which that space is divided. We define the statistic Ω (t) (Eq. (7)) as the instantaneous Shannon entropy of the simplex, normalized by its maximum, uniquely associated with the equiprobable distribution $p_{\kappa\ (t)} = \frac{1}{N}, \forall\ \kappa \in \{1; \ldots; N\}$.

$$\Omega\ (t) = -\frac{\sum_{\kappa=1}^{N}[p_{\kappa\ (t)} \ln\ (p_{\kappa\ (t)})]}{\ln\ (N)} \qquad (7)$$

The magnitude Ω (t) thus takes real values between 0 and 1. We can associate the Ω (t) statistic with histograms determined from the particles axial distribution after starting their path in a given voxel, as illustrated in Fig. 12. Using the manifold of trajectories, a probability simplex can be constructed over the distance to the midpoint of the starting voxel. The probability distributions have a systematic tendency to evolve to a fixed form, an absolute convergence, dependent only on the operating conditions. After a while, these distributions do not differ from each other and correspond to an asymptotic value of the Ω (t) statistic.

Fig. 12, 13

Fig. 13 shows the temporal evolution of the Normalized Shannon Entropy time-series Ω (*t*) concerning the dispersion of trajectories that start from the same point. It is observed that the quantifier Ω (*t*) reaches an asymptotic value less than one because it is related to the distribution of the solid phase that is established once the pseudo-steady state is reached for a given operating condition. This asymptotic value corresponds to the maximum level of mixing of the phase that the tracer represents within the system.

Taking into account that the dependence of the Shannon entropy with time reaches a stationary value (or plateau) regardless of the "injection point" where the trajectories started (Salierno et al., 2018), it can be possible to determine the mixing time of solids by finding the first portion of the curve where the product of the slope and the linear regression correlation coefficient approximates significantly to zero, verifying that the normalized entropy value does not differ significantly from the plateau value. Experimental and simulated mixing times are compared for every liquid velocity condition, as shown in Fig. 14.

Fig. 14

The mixing time values obtained from simulations are in the same order of magnitude as those observed by RPT. It should be noted that the simulated mixing times are about 25% lower than the experimental, which is a fair prediction considering that the mixing time value might differ depending on the algorithm implemented to find the plateau and the tolerance threshold applied to the slope of Ω (*t*).

5 Conclusions

The motion of a tracer resembling calcium alginate spheres induced by the upward flow of water in a liquid–solid fluidized bed column was examined with RPT and has been compared to those estimated from CFD-DEM simulations. Despite the additional research work required to fully capture the details of the emergent behavior, the model can reasonably describe the solid phase distribution and velocity fields far from the column entrance. The simulation does not properly capture the entrance region, especially positions close to the column wall; hence, these results would better be applied to fluidized beds with liquid holdup or bed porosity larger than 0.8. For these conditions, the particles' motion dynamics above a bed diameter length are well captured by the simulations, and parameters used to represent particles dispersion and mixing are properly estimated. Moreover, the simulations successfully predict a flow transition observed in the experimental data without fitting parameters.

A fairly good agreement is found between the predicted and experimental solid dynamic motion as inferred from time series analysis. The Diks' test was used to decide if two sets of trajectories have the same dynamic origin. The S-statistic used to compare time series indicates that the underlying dynamics of

the simulated data match the experimental data for the same condition. Apart from indicating that the model properly captures the system dynamics, the S-statistic calculated only from simulated data can predict the inception of a region of smooth homogeneous fluidization, with low particle–particle interactions that end with particle entrainment. The correlation dimension and Kolmogorov entropy trends with the liquid velocity are less conclusive in diagnosing the flow transition.

Moreover, the simulation accurately predicted solid dispersion coefficients, a widely used quantity in chemical reactor design. Information entropy obtained from the manifold of trajectories was employed for the quantitative determination of mixing times; values predicted from simulations are found to differ less than 25% from those calculated from the experiments. The high similarity observed in the asymptotic Shannon entropy values suggests that experimental and simulated solid distributions are allowed states of liquid fluidization under the explored conditions.

Acknowledgments

We would particularly like to thank the staff of the RA1 reactor of CNEA, Argentina, for activating the sources used in this work. Financial support from Högskolestiftelsen i Österbotten (2804720/28600122), the Harry Schaumans Foundation (2804720/28002257), Suomen Kulttuurirahasto (00210970), CONICET (PIP1122015-0100902CO), and Universidad de Buenos Aires (UBACyT 20020130100544BA) is gratefully acknowledged.

References

Ali, N., Al-Juwaya, T., Al-Dahhan, M., 2015. Detailed 3D solids dynamics of gas-solid spouted beds using gamma ray computed tomography (CT) and radioactive particle tracking (RPT) techniques. Presented at the Transactions of the American Nuclear Society, pp. 402–405.

Al-Juwaya, T., Ali, N., Al-Dahhan, M., 2019. Investigation of hydrodynamics of binary solids mixture spouted beds using radioactive particle tracking (RPT) technique. Chemical Engineering Research and Design 148, 21–44. https://doi.org/10.1016/j.cherd.2019.05.051

Bennacef, C., Desobry-Banon, S., Probst, L., Desobry, S., 2021. Advances on alginate use for spherification to encapsulate biomolecules. Food Hydrocolloids 118, 106782. https://doi.org/10.1016/j.foodhyd.2021.106782

Cassanello, M., Larachi, F., Marie, M.-N., Guy, C., Chaouki, J., 1995. Experimental Characterization of the Solid Phase Chaotic Dynamics in Three-Phase Fluidization. Ind. Eng. Chem. Res. 34, 2971–2980. https://doi.org/10.1021/ie00048a007

Chaouki, J., Larachi, F., Dudukovic, M.P. (Eds.), 1997. Non-invasive monitoring of multiphase flows. Elsevier, Amsterdam ; New York.

Di Felice, R., 1995. Hydrodynamics of liquid fluidisation. Chemical Engineering Science 50, 1213–1245. https://doi.org/10.1016/0009-2509(95)98838-6

Diks, C., van Zwet, W.R., Takens, F., DeGoede, J., 1996. Detecting differences between delay vector distributions. Phys. Rev. E 53, 2169–2176. https://doi.org/10.1103/PhysRevE.53.2169

Duduković, M., Mills, P., 2015. Scale-up and multiphase reaction engineering. Current Opinion in Chemical Engineering, Energy and environmental engineering • Reaction engineering and catalysis 9, 49–58. https://doi.org/10.1016/j.coche.2015.08.002

Ebrahimi-Mamaghani, A., Sotudeh-Gharebagh, R., Zarghami, R., Mostoufi, N., 2019. Dynamics of two-phase flow in vertical pipes. Journal of Fluids and Structures 87, 150–173. https://doi.org/10.1016/j.jfluidstructs.2019.03.010

Ercole, A., Raganati, F., Salatino, P., Marzocchella, A., 2021. Continuous succinic acid production by immobilized cells of Actinobacillus succinogenes in a fluidized bed reactor: Entrapment in alginate beads. Biochemical Engineering Journal 169, 107968. https://doi.org/10.1016/j.bej.2021.107968

Fraguío, M.S., Cassanello, M.C., Larachi, F., Limtrakul, S., Dudukovic, M., 2007. Classifying flow regimes in three-phase fluidized beds from CARPT experiments. Chemical Engineering Science 62, 7523–7529. https://doi.org/10.1016/j.ces.2007.08.039

Goniva, C., Kloss, C., Deen, N.G., Kuipers, J.A.M., Pirker, S., 2012. Influence of rolling friction on single spout fluidized bed simulation. Particuology 10, 582–591. https://doi.org/10.1016/j.partic.2012.05.002

Hager, A., Kloss, C., Goniva, C., 2018. Combining Open Source and Easy Access in the field of DEM and coupled CFD-DEM: LIGGGHTS®, CFDEM®coupling and CFDEM®workbench, in: Friedl, A., Klemeš, J.J., Radl, S., Varbanov, P.S., Wallek, T. (Eds.), Computer Aided Chemical Engineering, 28 European Symposium on Computer Aided Process Engineering. Elsevier, pp. 1699–1704. https://doi.org/10.1016/B978-0-444-64235-6.50296-5

Hager, A., Kloss, C., Pirker, S., Goniva, C., 2014. Parallel Resolved Open Source CFD-DEM: Method, Validation and Application. The Journal of Computational Multiphase Flows 6, 13–27. https://doi.org/10.1260/1757-482X.6.1.13

Hua, L., Lu, L., Yang, N., 2020. Effects of liquid property on onset velocity of circulating fluidization in liquid-solid systems: A CFD-DEM simulation. Powder Technology 364, 622–634. https://doi.org/10.1016/j.powtec.2020.01.051

Kalo, L., Pant, H.J., Cassanello, M.C., Upadhyay, R.K., 2019. Time series analysis of a binary gas-solid conical fluidized bed using radioactive particle tracking (RPT) technique data. Chemical Engineering Journal 377, 119807. https://doi.org/10.1016/j.cej.2018.08.193

Khan, Md.S., Evans, G.M., Nguyen, A.V., Mitra, S., 2020. Analysis of particle dispersion coefficient in solid-liquid fluidised beds. Powder Technology 365, 60–73. https://doi.org/10.1016/j.powtec.2019.03.022

Kramer, O.J.I., de Moel, P.J., Baars, E.T., van Vugt, W.H., Padding, J.T., van der Hoek, J.P., 2019. Improvement of the Richardson-Zaki liquid-solid fluidisation model on the basis of hydraulics. Powder Technology 343, 465–478. https://doi.org/10.1016/j.powtec.2018.11.018

Lee, B.-B., Ravindra, P., Chan, E.-S., 2013. Size and Shape of Calcium Alginate Beads Produced by Extrusion Dripping. Chem. Eng. Technol. n/a-n/a. https://doi.org/10.1002/ceat.201300230

Lichtenegger, T., 2018. Local and global recurrences in dynamic gas-solid flows. International Journal of Multiphase Flow 106, 125–137. https://doi.org/10.1016/j.ijmultiphaseflow.2018.05.013

Liu, M., Liu, L., Zhang, H., Yi, B., Everaert, N., 2021. Alginate oligosaccharides preparation, biological activities and their application in livestock and poultry. Journal of Integrative Agriculture 20, 24–34. https://doi.org/10.1016/S2095-3119(20)63195-1

Maestri, M., Salierno, G., Piovano, S., Cassanello, M., Cardona, M.A., Hojman, D., Somacal, H., 2019. CFD-DEM modeling of solid motion in a water-calcium alginate fluidized column and its comparison with results from radioactive particle tracking. Chemical Engineering Journal 377. https://doi.org/10.1016/j.cej.2018.11.037

Monin, A.S., Jaglom, A.M., Lumley, J.L., 1981. Statistical fluid mechanics: mechanics of turbulence. Bd. 2: Statistical fluid mechanics: mechanics of turbulence, 2. Aufl. ed. MIT Press, Cambridge.

Platero, E., Fernandez, M.E., Bonelli, P.R., Cukierman, A.L., 2017. Graphene oxide/alginate beads as adsorbents: Influence of the load and the drying method on their physicochemical-mechanical properties and adsorptive performance. Journal of Colloid and Interface Science 491, 1–12. https://doi.org/10.1016/j.jcis.2016.12.014

Roy, S., 2017. Radiotracer and particle tracking methods, modeling and scale-up. AIChE J. 63, 314–326. https://doi.org/10.1002/aic.15559

Roy, S., Kemoun, A., Al-Dahhan, M.H., Dudukovic, M.P., Skourlis, T.B., Dautzenberg, F.M., 2005. Countercurrent flow distribution in structured packing via computed tomography. Chemical Engineering and Processing: Process Intensification 44, 59–69. https://doi.org/10.1016/j.cep.2004.03.010

Salierno, G., Maestri, M., Piovano, S., Cassanello, M., Cardona, M.A., Hojman, D., Somacal, H., 2018. Solid motion in a three-phase bubble column examined with Radioactive Particle Tracking. Flow Measurement and Instrumentation 62, 196–204. https://doi.org/10.1016/j.flowmeasinst.2017.10.002

Salierno, G.L., Maestri, M., Piovano, S., Cassanello, M., Cardona, M.A., Hojman, D., Somacal, H., 2013. Discrete axial motion of a radioactive tracer reconstructed from the response of axially aligned detectors: Application to the analysis of a bubble column dynamics. Chemical Engineering Science 100, 402–412. https://doi.org/10.1016/j.ces.2013.03.029

Schouten, J.C., Takens, F., van den Bleek, C.M., 1994a. Maximum-likelihood estimation of the entropy of an attractor. Phys. Rev. E 49, 126–129. https://doi.org/10.1103/PhysRevE.49.126

Schouten, J.C., Takens, F., van den Bleek, C.M., 1994b. Estimation of the dimension of a noisy attractor. Phys. Rev. E 50, 1851–1861. https://doi.org/10.1103/PhysRevE.50.1851

Sheikhi, A., Sotudeh-Gharebagh, R., Mostoufi, N., Zarghami, R., 2013. Frequency-based characterization of liquid–solid fluidized bed hydrodynamics using the analysis of vibration signature and pressure fluctuations. Powder Technology 235, 787–796. https://doi.org/10.1016/j.powtec.2012.11.026

Sutirman, Z.A., Sanagi, M.M., Wan Aini, W.I., 2021. Alginate-based adsorbents for removal of metal ions and radionuclides from aqueous solutions: A review. International Journal of Biological Macromolecules 174, 216–228. https://doi.org/10.1016/j.ijbiomac.2021.01.150

Takens, F., 1981. Detecting strange attractors in turbulence, in: Rand, D., Young, L.-S. (Eds.), Dynamical Systems and Turbulence, Warwick 1980, Lecture Notes in Mathematics. Springer Berlin Heidelberg, Berlin, Heidelberg, pp. 366–381. https://doi.org/10.1007/BFb0091924

Van den Broeck, C., Esposito, M., 2015. Ensemble and trajectory thermodynamics: A brief introduction. Physica A: Statistical Mechanics and its Applications, Proceedings of the 13th International Summer School on Fundamental Problems in Statistical Physics 418, 6–16. https://doi.org/10.1016/j.physa.2014.04.035

van Ommen, J.R., Coppens, M.-O., van den Bleek, C.M., Schouten, J.C., 2000. Early warning of agglomeration in fluidized beds by attractor comparison. AIChE J. 46, 2183–2197. https://doi.org/10.1002/aic.690461111

van Ommen, J.R., Sasic, S., van der Schaaf, J., Gheorghiu, S., Johnsson, F., Coppens, M.-O., 2011. Time-series analysis of pressure fluctuations in gas–solid fluidized beds – A review. International Journal of Multiphase Flow 37, 403–428. https://doi.org/10.1016/j.ijmultiphaseflow.2010.12.007

Wang, B., Zhang, Q., Hong, J., Li, L., 2018. Highly effective iron–carbon–bentonite–alginate beads (Fe°/C-BABs) as catalyst to treat benzalkonium chloride in fixed-bed column systems. Process Safety and Environmental Protection 119, 75–86. https://doi.org/10.1016/j.psep.2018.07.018

Wang, M., 2015. Industrial tomography: systems and applications. Elsevier, Boston, MA.

Wang, S., Guo, S., Gao, J., Lan, X., Dong, Q., Li, X., 2012. Simulation of flow behavior of liquid and particles in a liquid–solid fluidized bed. Powder Technology 224, 365–373. https://doi.org/10.1016/j.powtec.2012.03.022

Zhang, J., Chen, X., Hou, J., Zhang, W., Wu, S., 2021. Early risk warning method for fluidized beds using generalized extremum distribution of pressure fluctuation. Process Safety and Environmental Protection 156, 29–42. https://doi.org/10.1016/j.psep.2021.09.037

Zou, Y., Donner, R.V., Marwan, N., Donges, J.F., Kurths, J., 2019. Complex network approaches to nonlinear time series analysis. Physics Reports 787, 1–97. https://doi.org/10.1016/j.physrep.2018.10.005

Fig. 1. Experimental setup scheme (left) and a detail of the column (right).

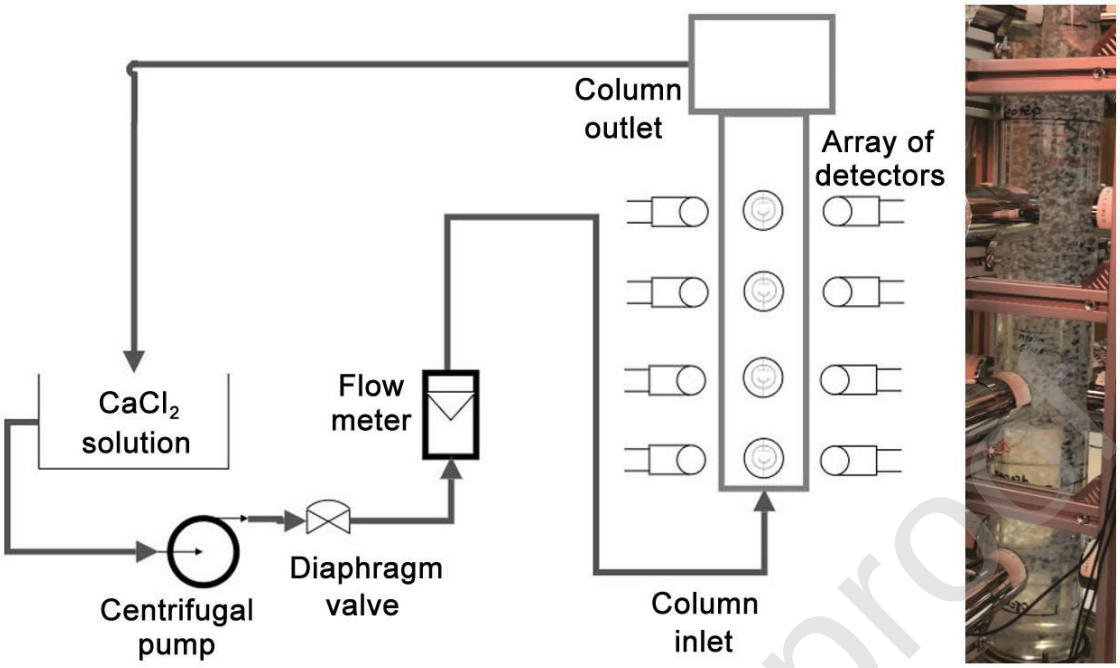

Fig. 2. Experimental (left) and Simulated (right) solid hold-up distribution: (a) Radially averaged axial profile; (b) Axially averaged radial profile; (c) Axially averaged radial profile at the column base (z/D < 1).

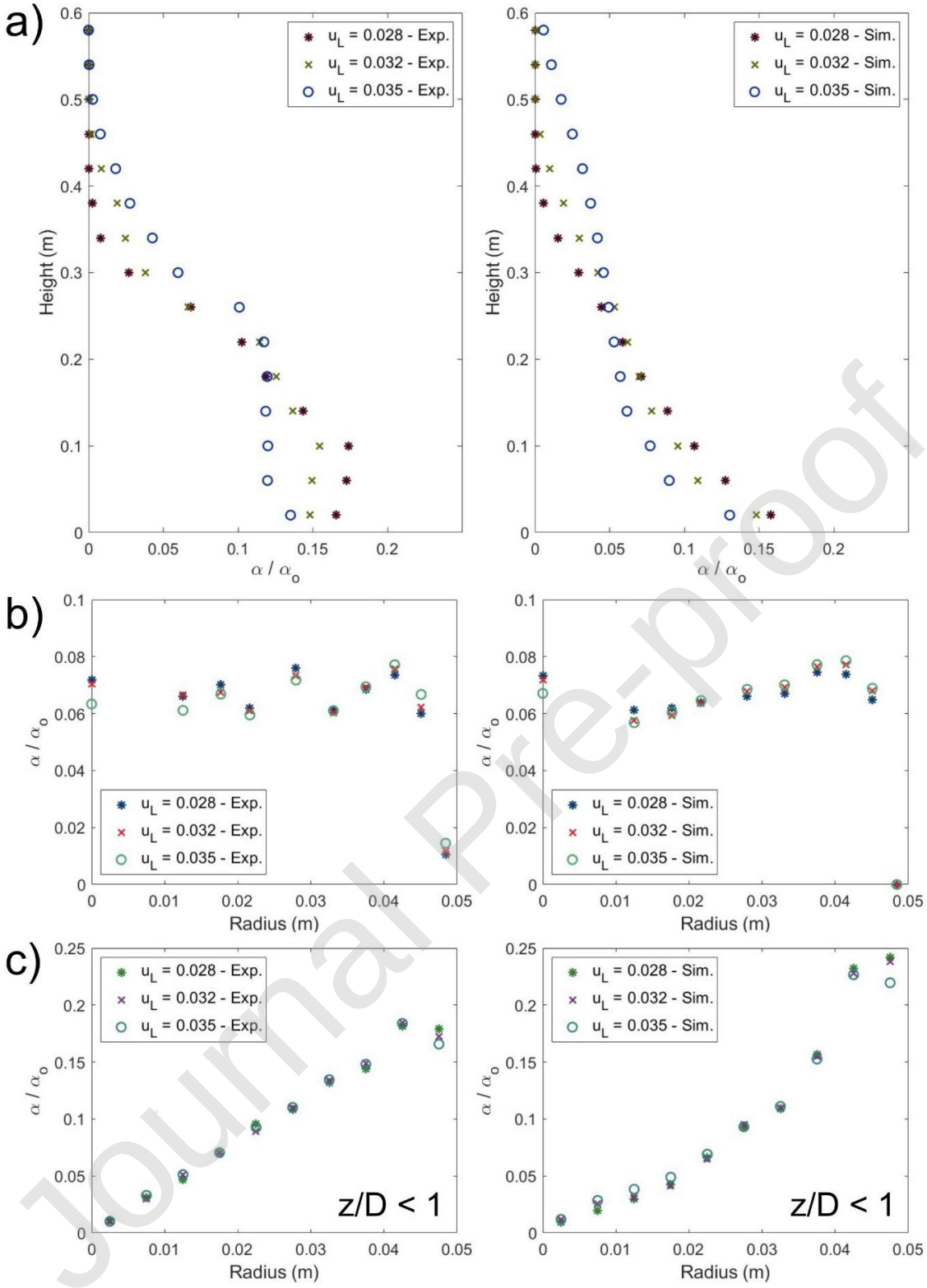

Fig. 3. Experimental (above) and simulated (below) time-averaged velocity fields (azimuthal projection).

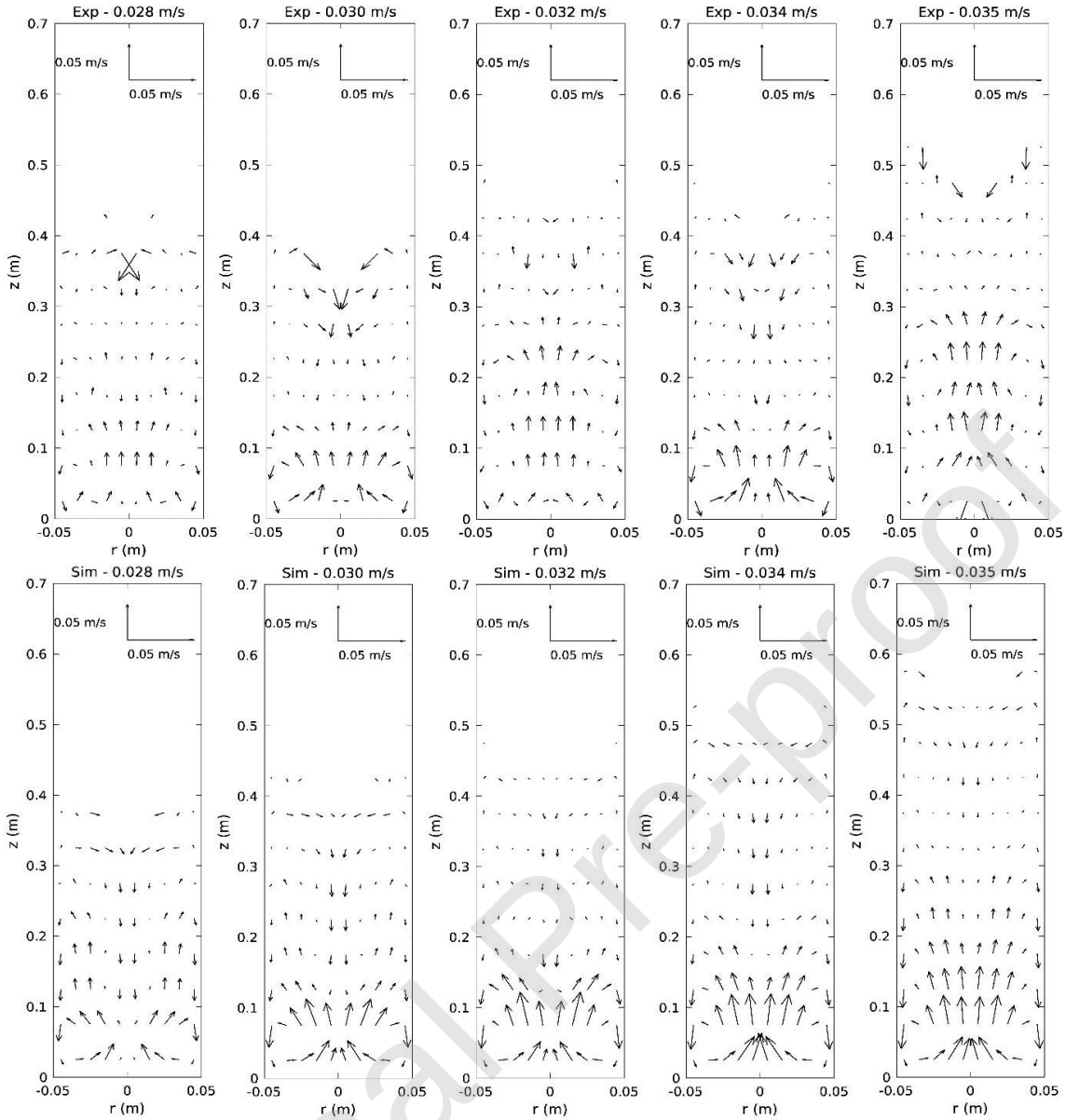

Fig. 4. S-statistic results from the comparison within the experimental data. The dotted line denotes the cut-off of the Diks' test, following the 3σ rule.

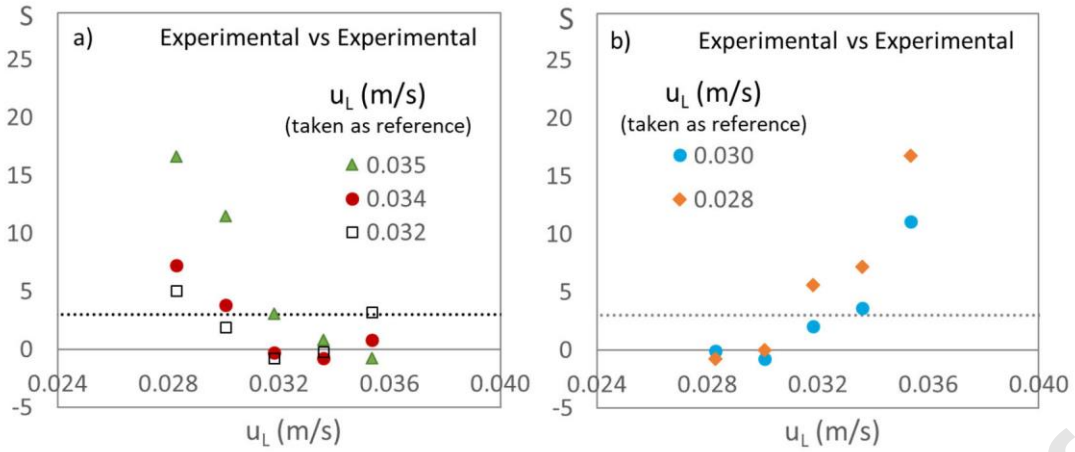

Fig. 5. S-statistic results from comparing the simulated and the experimental data. The dotted line denotes the cut-off of the Diks' test, following the 3σ rule.

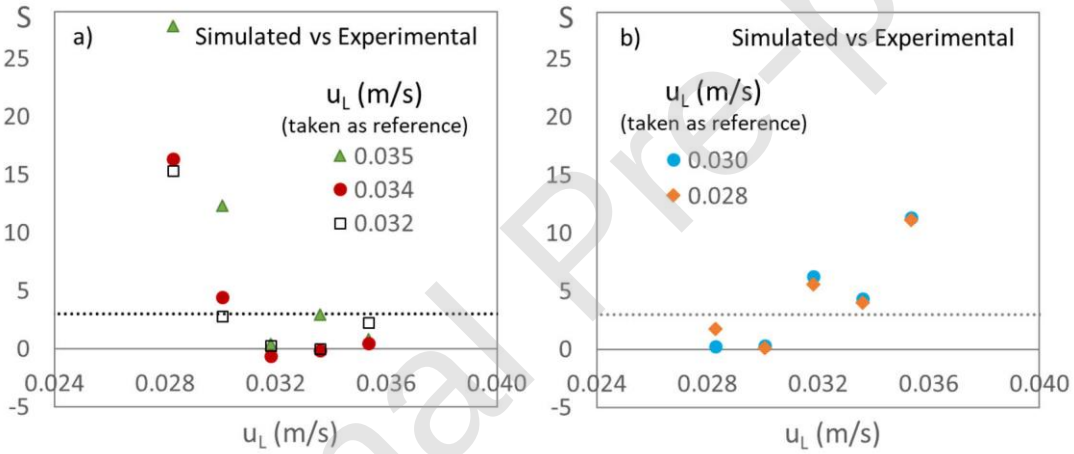

Fig. 6. S-statistic results from the comparison within the extended ranged simulations. Dotted line denotes the cut-off of the Diks' test, following the 3σ rule.

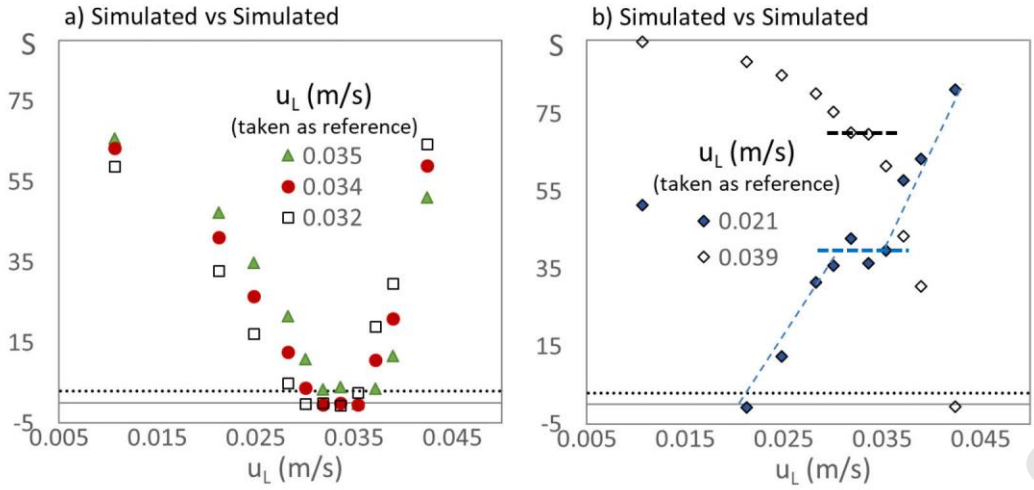

Fig. 7. Snap-shots of the simulated fluidized bed at an instant after 3 minutes for a broad liquid velocity range before particle entrainment.

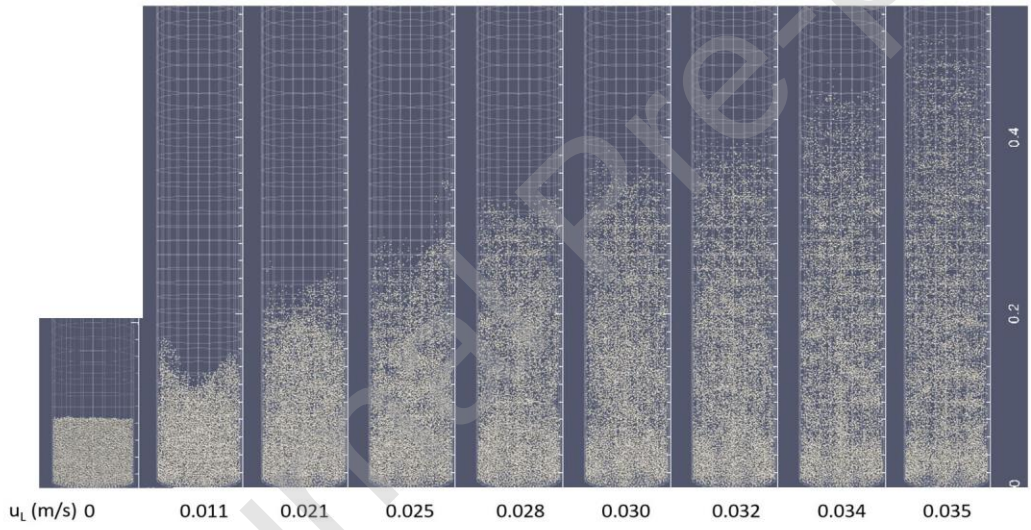

Fig. 8. Photographs of different regions of the fluidized bed for the lowest and highest liquid velocities examined with RPT.

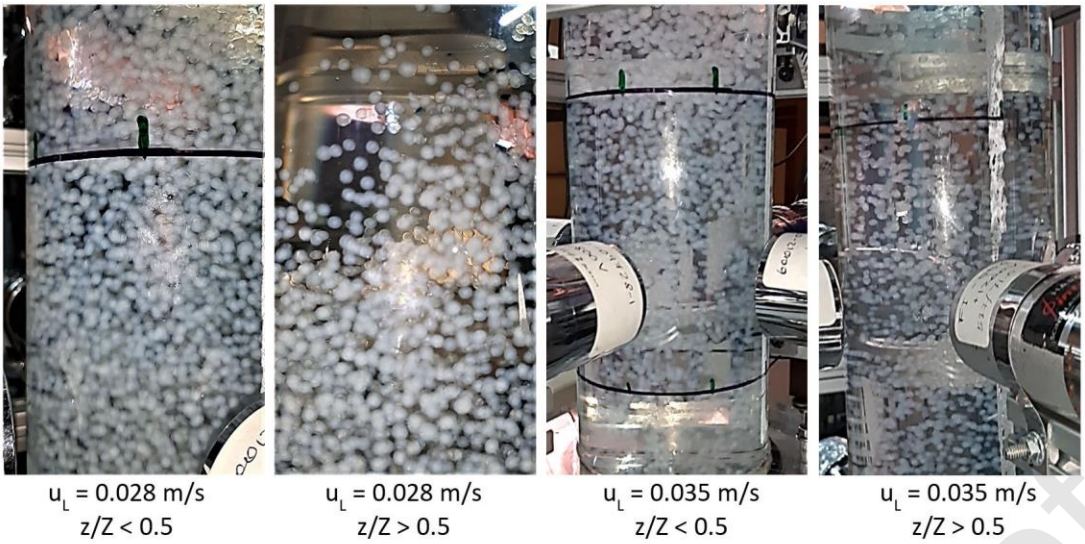

Fig. 9. Correlation dimension and Kolmogorov entropy determined from the moving particle axial coordinate time series obtained by RPT or CFD-DEM simulations.

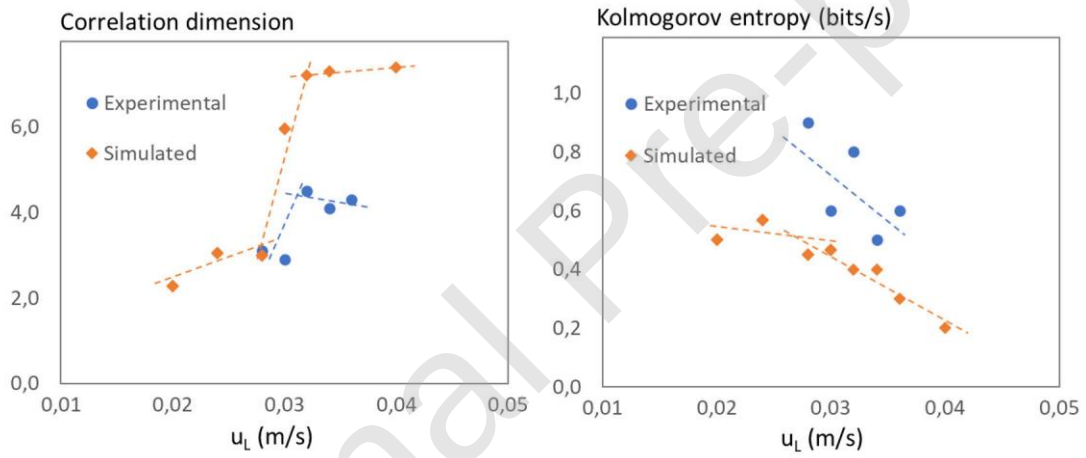

Fig. 10. Mean squared displacement of a manifold as a function of time. Black dots depict the linear zone where the dispersion coefficient is obtained.

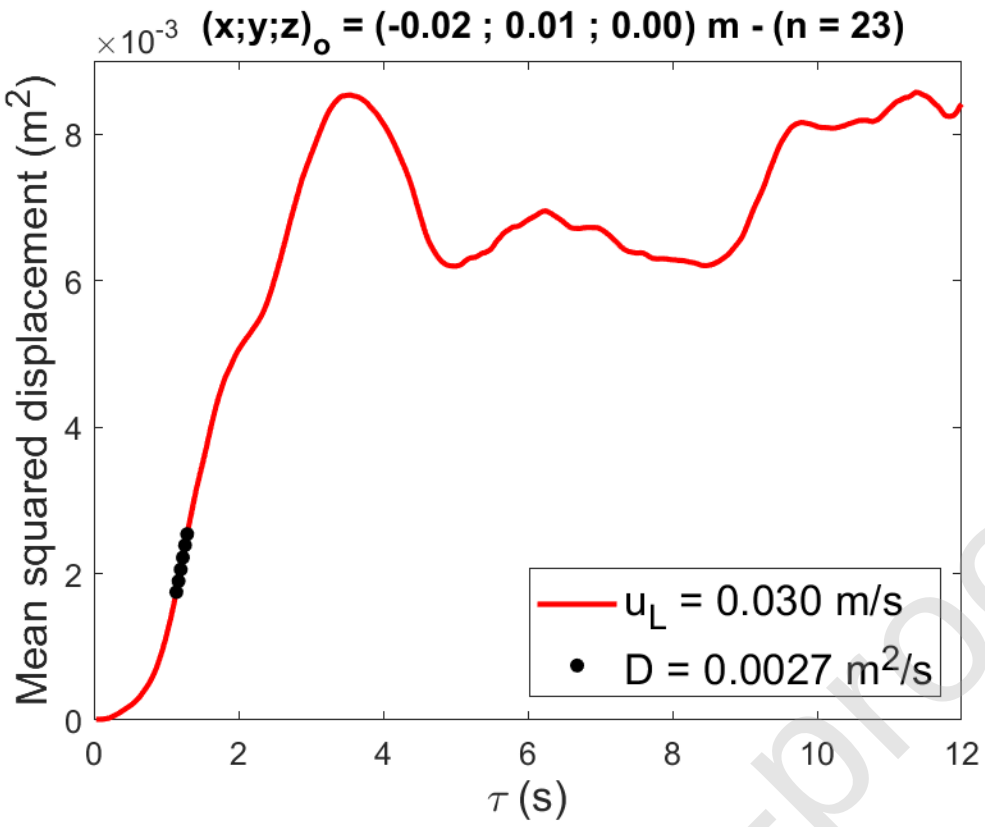

Fig. 11. Experimental solid dispersion coefficients are accurately predicted by the simulation.

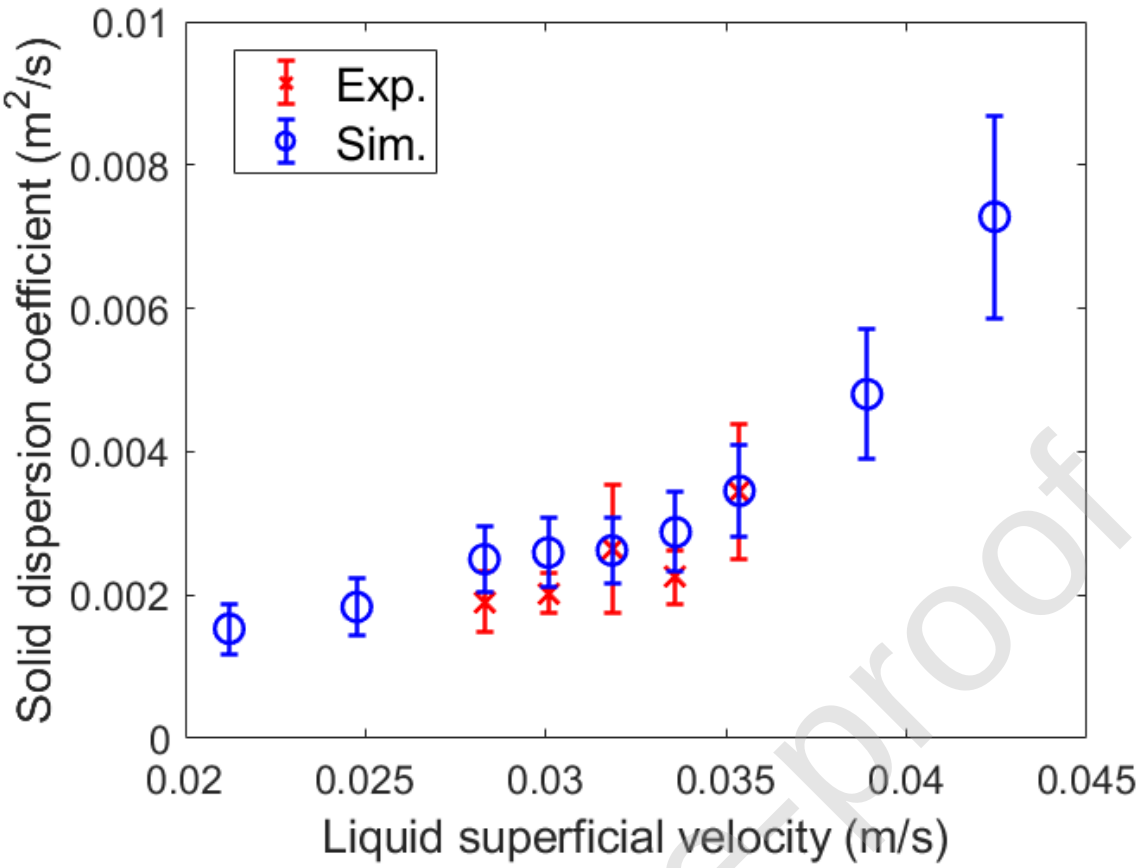

Fig. 12. Histograms corresponding to the distance from starting point at different times: 0; 0.1; 1; 2; 5; 10 and 20 s.

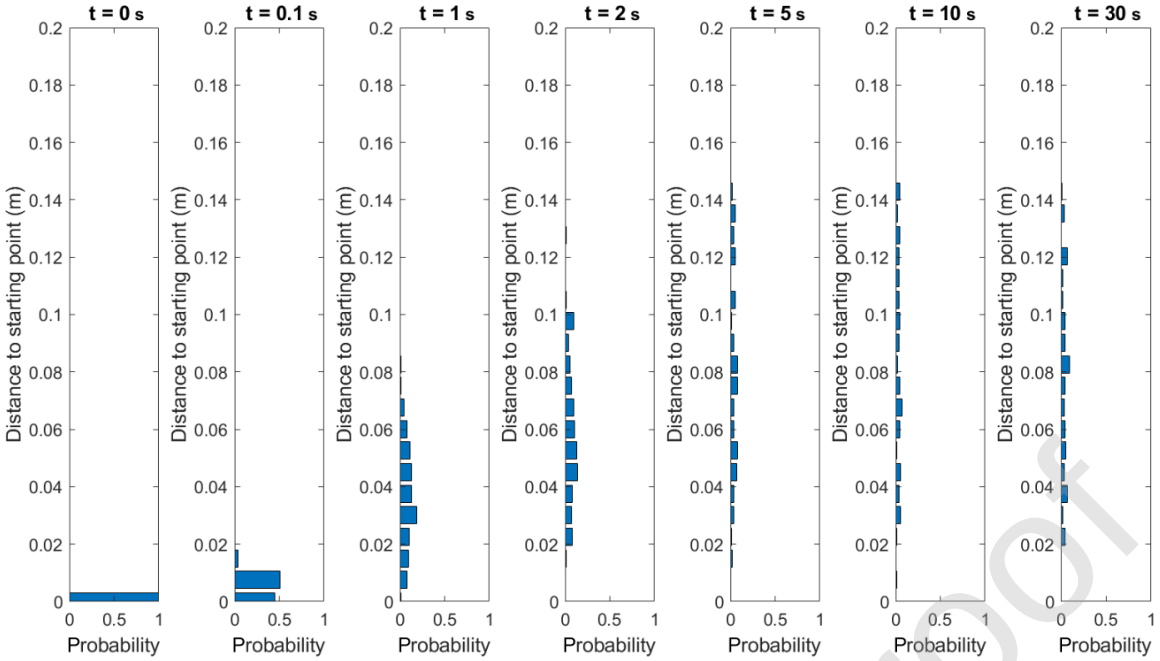

Fig. 13. Normalized Shannon entropy evolution with time.

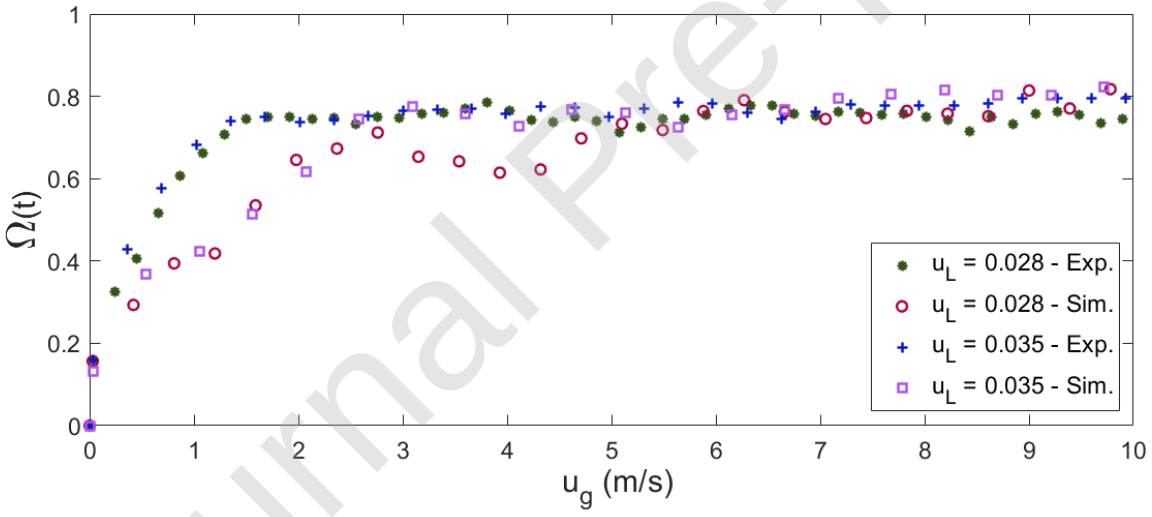

Fig. 14. Comparison of the experimental and simulated mixing times.

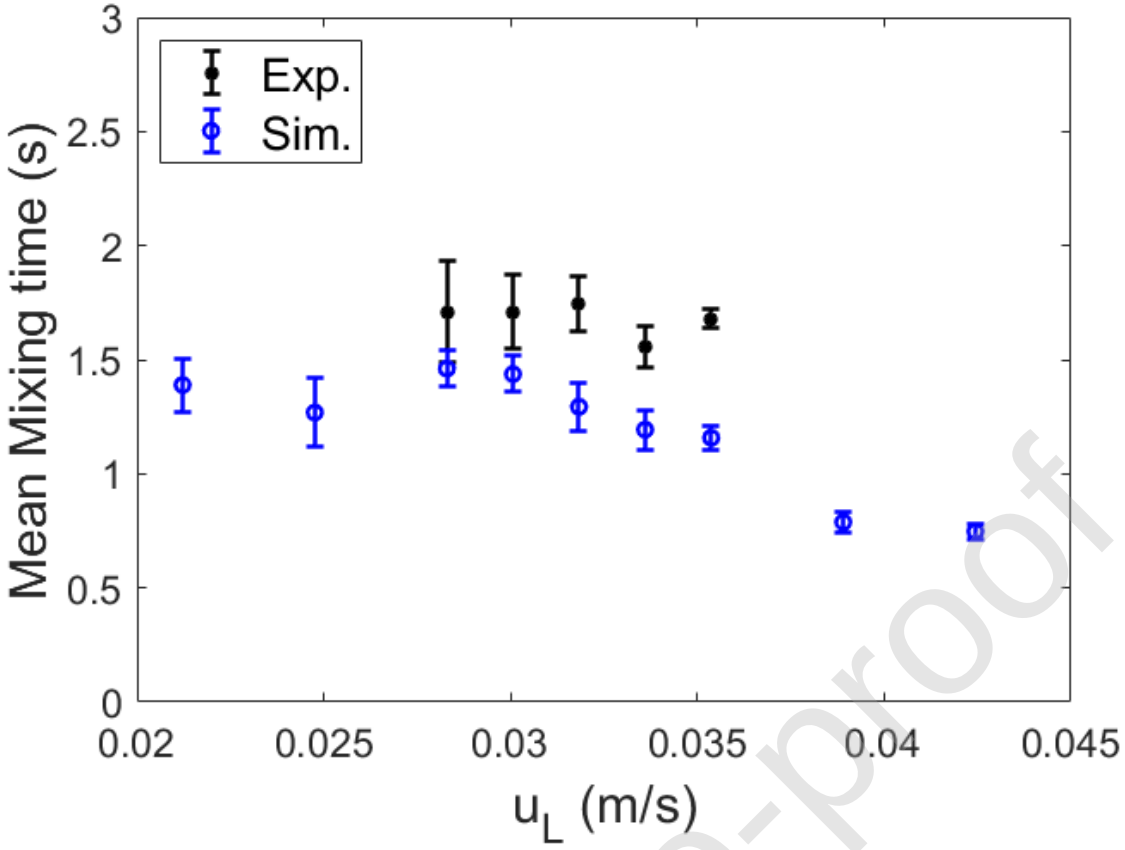

Table 1 Relevant physical properties of the phases and radioactive tracer.

Component	Parameter	Values
$CaCl_2$ (aq.) 0.05 M	Density	1008 kg/m^3
	Viscosity	1.02 mPa·s
	Superficial velocity	0.028–0.036 m/s
	Distributor hole velocity	1.42–1.77 m/s
Calcium alginate particles	Density	1030 kg/m^3
	Mean diameter	4 mm
	Young modulus	200 kPa
	Poisson Ratio	0.5
Radioactive tracer	Density	1028 kg/m^3
	Diameter	3.8 mm
	Activity	30 µCi

Table 2 Forces acting over the solid particles.

Expression	Physical meaning
$m_i \frac{\delta \mathbf{v_i}}{\delta t} = m_i \mathbf{g} + \mathbf{f_{pL,i}} + \sum_{j \neq i}^{\#coll.} (\mathbf{f_{c,ij}} + \mathbf{f_{e,ij}})$	Force balance over the i-th particle
$\mathbf{f_{pL,i}} = \mathbf{f_{\nabla p,i}} + \mathbf{f_{d,i}} + \mathbf{f_{\nabla \cdot \tau,i}}$	Particle–liquid interactions
$\mathbf{f_{\nabla p,i}} = -\mathrm{V}_{p,i} (\boldsymbol{\nabla} \mathbf{p})$	Pressure gradient force
$\mathbf{f_{\nabla \cdot \tau,i}} = -\mathrm{V}_{p,i} (\boldsymbol{\nabla} \cdot \boldsymbol{\tau})$ $\boldsymbol{\tau} = \mu_L [\boldsymbol{\nabla} \mathbf{u} + (\boldsymbol{\nabla} \mathbf{u})^{-1}]$	Shear force
$\mathbf{f_{d,i}} = 0{,}125 \cdot C_d \cdot \rho_L \pi d_i^2 \varepsilon_i^{2-\chi} \cdot \lvert \mathbf{u} - \mathbf{v_i} \rvert (\mathbf{u} - \mathbf{v_i})$ $C_d = \left(0{,}63 + \frac{4{,}8}{Re_{p,i}^{1/2}} \right)^2 ; Re_{p,i} = \frac{\rho_L d_{p,i} \varepsilon_i \lvert \mathbf{u} - \mathbf{v_i} \rvert}{\mu_L}$ $\chi = 3{,}7 - 0{,}65 \cdot e^{-0{,}5 \cdot \left(1{,}5 - log\left(Re_{p,i}\right)\right)^2}$	Drag force (Di Felice, 1995)
$\mathbf{f_{c,ij}}$	Interparticle plastic collision term
$\mathbf{f_{e,ij}}$	Interparticle elastic collision term

Table 3 Simulation settings

Parameter	Value	Unit
Column diameter	0.1	m
Column length	1	m
Number of particles	13500	beads
Particle mean diameter	3.8	mm
Young modulus	200	kPa
Coefficient of restitution	0.3	
Particle density	1025	kg/m^3
Initial bed height	0.5	m
Initial voidage	0.9	
Outlet boundary condition	Fully developed flow	
Wall boundary condition	No-slip	
Gravitational acceleration	9.81	m/s^2
Operating pressure	1	atm

CFD-DEM characteristics

Mesh type	structured hexahedral	
Mesh size (average volume)	0.9	cm^3
Mesh number	8640	
Time step (CFD)	2×10^{-4}	s
Time step (LIGGGHTS)	1×10^{-5}	s
Calculation time	380	s / (simul. s)
Courant number (typical)	4×10^{-4}	
Courant number (max.)	3.5×10^{-3}	
Step iteration number	6	iterations
CFL number	10^{-7} to 10^{-4}	

Table 4 S-statistic for comparison within simulated data. Dynamic similarity hypothesis is accepted mostly in the diagonal.

u_L (m/s)	0.011	0.021	0.025	0.028	0.030	0.032	0.034	0.035	0.037	0.039	0.042
0.011	–0.5	55.7	74.4	79.9	69.9	69.7	62.4	59.9	72.5	74.9	87.0
0.021	51.5	–0.7	12.3	31.6	35.8	42.7	36.4	39.8	57.9	63.4	81.4
0.025	77.9	17.5	–0.6	7.2	15.7	25.4	20.7	27.3	48.2	55.7	77.9
0.028	71.8	26.7	4.7	–0.4	4.6	13.1	9.9	17.2	39.0	48.0	73.9
0.030	63.8	32.3	13.8	1.9	–0.7	2.3	1.3	6.6	26.2	36.9	68.6
0.032	58.9	32.9	17.3	5.0	–0.1	–0.1	–0.5	2.6	19.0	29.7	64.4
0.034	63.4	41.1	26.5	12.8	3.9	–0.3	0.0	–0.3	10.7	21.0	59.0
0.035	65.7	47.3	34.9	21.6	10.9	3.5	3.9	–0.2	3.7	11.7	51.0
0.037	59.5	43.2	32.8	21.5	12.2	5.1	5.3	0.5	1.9	8.1	44.9
0.039	66.8	54.7	46.8	37.3	28.1	19.1	19.2	10.0	0.1	–0.1	27.6
0.042	93.7	88.4	84.9	80.3	75.6	70.1	69.7	61.6	43.4	30.5	–0.5